Flexible chiral pyrazolate-based metal–organic framework containing saddle-type CuI 4(pyrazolate)4 units

Maciej Grzywa, Dmytro Denysenko, Andreas Schaller, Andreas Kalytta-Mewes, Dirk Volkmer

Flexible chiral pyrazolate-based metal–organic framework containing saddle-type Cu$^I_4$(pyrazolate)$_4$ units†

Maciej Grzywa, Dmytro Denysenko, Andreas Schaller, Andreas Kalytta-Mewes and Dirk Volkmer*

The syntheses and crystal structures of [Cu$^I_2$(phbpz)]·MeOH (**lp-CFA-9**, lp = large-pore) and [Cu$^I_2$(phbpz)] (**np-CFA-9**, np = narrow-pore; H$_2$-phbpz = 3,3′,5,5′-tetraphenyl-1H,1′H-4,4′-bipyrazole) are described. The copper(I)-containing metal–organic framework (termed Coordination Framework Augsburg University-9, **lp-CFA-9**) crystallizes in the trigonal crystal system, within the chiral space group $P3_221$ (no. 154) and with the following unit cell parameters: a = 18.2348(6), c = 16.3950(4) Å, and V = 4721.1(2) Å^3. **Lp-CFA-9** features a 3-D microporous framework structure of Cu$_4$pz$_4$ (pz = pyrazolate) SBUs with the D_{2d} (= $\bar{4}2m$) symmetry connected by single bonds creating one-dimensional channels expanding in the c-direction of the crystal lattice. The framework flexibility of **CFA-9** has been demonstrated by single-crystal and powder X-ray analyses as well as by sorption measurements. **CFA-9** exhibits weak binding of carbon monoxide on Cu(I) centers. The reactivity of **CFA-9** towards oxidizing agents, such as H$_2$O$_2$, t-BuOOH and Br$_2$ was also investigated. Additionally, **CFA-9** shows luminescence upon exposure to UV radiation.

Introduction

During the last two decades, major efforts have been devoted to potential applications of metal–organic frameworks in catalysis,[1] gas storage and separation,[1c,2] drug delivery and biomedical imaging[3] and electrochemical energy storage.[4] Among about 20 000 MOF structures listed in the CSD, only about 100 compounds reveal substantial breathing transitions.[5] Breathing MOFs, which constitute a class of soft porous crystals (SPCs), feature a drastic change in unit cell volume (pore volume) upon the action of external stimuli such as guest molecule adsorption/desorption, temperature, pressure, light, and electric and magnetic fields.[6] Searching the literature by words using 'breathing MOF' in the databases SciFinder,[7] PubMed[8] and Web of Sciences[9] yields 69, 37 and 72 references, respectively. Among these, only two references give examples of chiral flexible MOFs, e.g. [La(BTB)(H$_2$O)·3DMF]$_n$ (H$_3$-BTB = 1,3,5-tris(4-carboxyphenyl)benzene),[10] and supramolecular MOFs (SMOFs) such as [Ca(L$_{ala}$)$_2$(H$_2$O)]·H$_2$O;

[Ca(L$_{ser}$)$_2$]·2H$_2$O; [Sr(L$_{ala}$)$_2$(H$_2$O)]·3H$_2$O; [Sr(L$_{ala*}$)$_2$(H$_2$O)]·3H$_2$O; and [Sr(L$_{ser}$)$_2$(H$_2$O)] (L$_{ala}$ = (S)-2-(1,8-naphthalimido)propanoate, L$_{ser}$ = (S)-2-(1,8-naphthalimido)-3-hydroxypropanoate, and L$_{ala*}$ = (R)-2-(1,8-naphthalimido)propanoate).[11] Chiral MOFs have attracted particular attention due to their potential applications in the fields of enantioselective catalysis,[12] chiral separation,[13] nonlinear optics,[14] and magnetism.[15]

On the other hand, copper-based MOFs have attracted particular interest, which relates to the role of copper centers in the active sites of metalloenzymes, such as oxidases or oxygenases.[16] Biologically inspired MOF catalysts hold great promise for a wide range of synthetic applications in the oxidation of organic intermediates containing non-activated C–H bonds. Few reports on applications of Cu-MOFs as oxidation catalysts have appeared in the literature. In particular, Cu-catalyzed hydroxylation of phenol,[17] oxidation of trimethylsilyl enolates to α-hydroxyketones,[18] allylic oxidation of cyclohexene,[19] cross-dehydrogenative coupling reactions of ethers with 2-carbonyl-substituted phenols,[20] oxidation of benzene derivatives and benzylic compounds[21] and arylation of heteroarenes[22] have been described.

Moreover, poly(azolate)-based MOFs (pyrazolate, imidazolate, triazolate, and tetrazolate) are often characterized by superior chemical and thermal stability as compared to their widespread carboxylate-based counterparts, the latter often exhibiting low stability against acidic or basic media and moisture.[23]

As part of our long-term research on functional Cu-MOFs, we have previously described the catalytic activity of CFA-5

Institute of Physics, Chair of Solid State and Materials Chemistry, Augsburg University, Universitaetsstrasse 1, 86159 Augsburg, Germany.
E-mail: dirk.volkmer@physik.uni-augsburg.de

† Electronic supplementary information (ESI) available: Ortep-style plot of the asymmetric units; topology analysis; XRPD patterns of **lp**- and **np-CFA-9**; and IR spectrum and gas sorption measurements of **CFA-9**. CCDC 1488850 and 1488851. For ESI and crystallographic data in CIF or other electronic format see DOI: 10.1039/c6ce01594h

(a Cu(II)-containing MOF) in the aerobic oxidation of tetralin[24] and the reactivity of Cu^I-MFU-4l towards C_2H_4 and CO.[25] Cu^I-MFU-4l contains highly reactive, coordinatively unsaturated (= "open") Cu(I)-metal sites, showing fully reversible chemisorption of small molecules such as O_2, N_2 or H_2 with high isosteric heats of adsorption. Our former studies on the reactivity of a Cu(I)-containing MOF CFA-2 toward molecular oxygen have shown that this compound is stable during the oxidation and reduction of the Cu ions, suggesting its potential usage in liquid-phase oxidation reactions.[26]

Here, we report on the synthesis and characterization of a new Cu(I)-MOF, termed CFA-9 (Coordination Framework Augsburg University-9), featuring a flexible 3-D microporous framework structure of Cu_4pz_4 (pz = pyrazolate) SBUs connected to each other by single bonds (Scheme 1). The Cu_4pz_4 structure motif is rather uncommon and only a few examples of crystalline compounds containing a Cu_4pz_4 unit can be found in the literature, e.g. a discrete metal complex $[Cu_4(HL^2)_2]$ (H_3L^2 = 1,3,5-tris((3,5-diphenyl-1H-pyrazol-4-yl)methyl)benzene)[27] and a metal–organic framework Cu_2L (L = 3,3′,5,5′-tetraethyl-4,4′-bipyrazolate) including two types of SBUs, namely, triangular Cu_3pz_3 units and saddle-type Cu_4pz_4 units.[28] The flexibility of the CFA-9 framework is demonstrated by single-crystal and powder X-ray analyses as well as by gas sorption measurements. CFA-9 is characterized by elemental and thermogravimetric analyses, variable temperature powder X-ray diffraction, and IR and luminescence spectroscopy. Additionally, the reactivity of CFA-9 towards oxidizing agents, such as H_2O_2, t-BuOOH and Br_2 is reported.

Results and discussion

Syntheses and characterization

The 3,3′,5,5′-tetraphenyl-1H,1′H-4,4′-bipyrazole ligand (H_2-phbpz) was synthesized according to a modified published procedure.[26,29] Lp-CFA-9 was synthesized by a solvothermal reaction starting from a Cu(II)-salt $Cu(OAc)_2 \cdot H_2O$ and a 3,3′,5,5′-tetraphenyl-1H,1′H-4,4′-bipyrazole ligand in a MeOH/2,6-lutidine system, giving colourless hexagonal prismatic crystals (Fig. 1).

Interestingly, slight changes of reaction conditions (a mixed-solvent system N,N-diethylformamide/EtOH/Et$_3$N was used instead of the aforementioned solvent) results in the formation of the Cu(I)-MOF CFA-2 (Scheme 1). CFA-2, featuring a 3-D three-connected two-fold interpenetrated porous structure constructed of triangular Cu(I) subunits and 3,3′,5,5′-tetraphenyl-1H,1′H-4,4′-bipyrazolate (phbpz) ligands, exhibits a pronounced breathing effect upon exposure to different guest molecules.

Additionally, applying microwave irradiation in the synthesis of CFA-9, instead of conventional heating, allowed us to reduce the reaction time drastically, from 3 d to 25 min.

Single crystal structure analysis

[Cu$^I_2$(phbpz)]·MeOH (lp-CFA-9). Lp-CFA-9 crystallizes in the trigonal crystal system within the chiral space group $P3_221$ (no. 154). The asymmetric unit consists of three copper, four nitrogen, thirteen carbon and twenty hydrogen atoms. An Ortep-style plot of the asymmetric unit of lp-CFA-9 is shown in the ESI,† Fig. S1. Lp-CFA-9 features a 3-D non-interpenetrated microporous structure constructed from Cu_4pz_4 secondary building units with the D_{2d} (= $\bar{4}2m$) symmetry, each containing a tetranuclear coordination unit of four Cu(I) ions and four pyrazolate ligands, as shown in Fig. 2a and b. The Cu(I) ions within each SBU are two-fold coordinated in a nearly linear arrangement by pyrazolate N-donor atoms from the ligand molecules; the N–Cu–N dihedral angles, therefore, are close to 180° (171.6(3), 172.9(2), 177.7(3)°). The four central Cu(I) ions are in the same plane, whereas two phbpz^{2-} ligands are positioned above and below this plane, thus building a saddle-shaped structure (see Fig. 2a). The intramolecular Cu⋯Cu distances range from 3.0252(7) to 3.1829(1) Å. The Cu–N distances range from 1.840(3) to 1.847(3) Å. These values are in good agreement with those found in the structurally related Cu-MOF, Cu_2L (L = 3,3′,5,5′-tetraethyl-4,4′-bipyrazolate),[28] and copper(I)-containing compounds.[27] The phenyl groups of each bipyrazolate linker are twisted with respect to each other and are disordered.
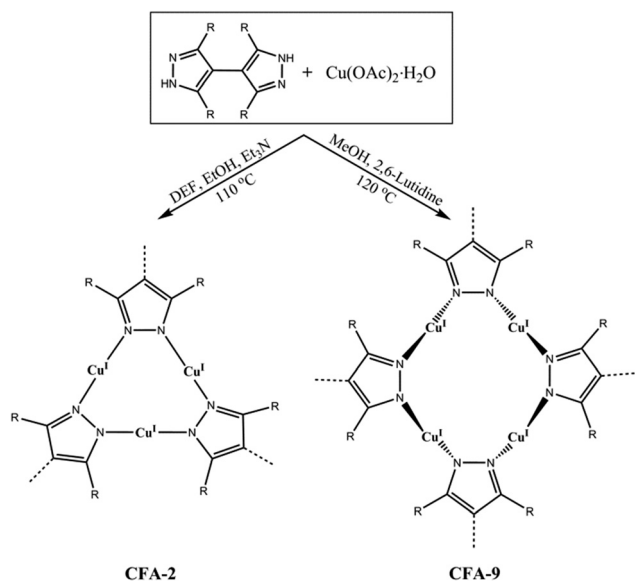
Scheme 1 Syntheses of [Cu$^I_2$(phbpz)]·2DEF·MeOH (**CFA-2**) and [Cu$^I_2$(phbpz)]·MeOH (**CFA-9**) from the H$_2$-phbpz ligand and copper(II) acetate (DEF = N,N-diethylformamide).
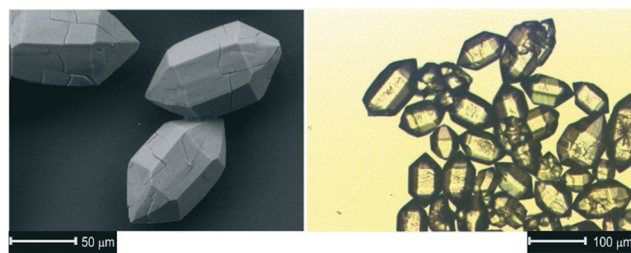

Fig. 1 SEM image (left) and optical micrograph (right) of **CFA-9** crystals.
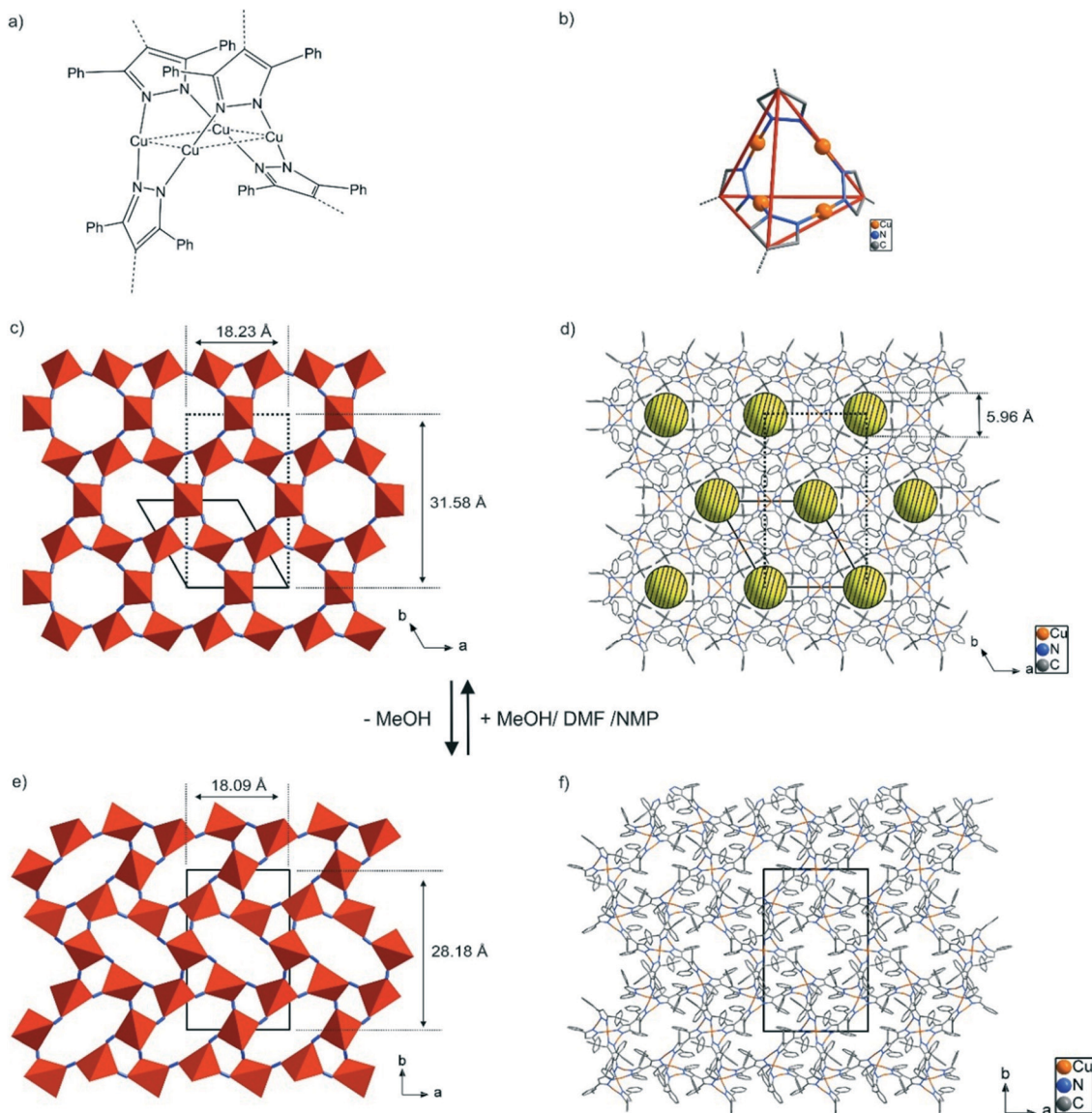
Fig. 2 (a) Coordination unit of the **CFA-9** framework featuring tetranuclear Cu(I) moieties. (b) Representation of the SBU of **CFA-9**. Phenyl groups were omitted for clarity. (c) Schematic packing diagram representing SBUs of **lp-CFA-9**, viewed in the *c*-direction. The dotted lines represent the unit cell of **lp-CFA-9** after transformation to the orthorhombic crystal system. (d) Packing diagram of **lp-CFA-9** with channels, viewed in the *c*-direction. Disordered phenyl rings and solvent molecules, as well as hydrogen atoms were omitted for clarity. (e) Schematic packing diagram representing SBUs of the desolvated phase of **np-CFA-9**, viewed in the *c*-direction. (f) Packing diagram of **np-CFA-9**, viewed in the *c*-direction.

The SBUs of **lp-CFA-9** are connected by single bonds and create one-dimensional channels expanding in the *c*-direction of the crystal lattice (see Fig. 2c and d). Taking the van der Waals radii of hydrogen atoms (1.2 Å) into account, the narrowest channel diameter calculated between the hydrogen atoms of the phenyl groups is 5.96 Å. Estimation using the SQUEEZE[30] program reveals that the initial solvent accessible void volume is 664.7 Å³, or 0.118 cm³ g⁻¹, which is 14.1% of the unit cell volume (4721.1(2) Å³) for a probe radius of 2.07 Å, corresponding to the approximate van der Waals radius of carbon dioxide.[31] In the crystal structure of **lp-CFA-9**, the channels are occupied by disordered MeOH molecules. The positions of the solvent molecules were impossible to resolve and refine from the electron density distribution. According

to the crystallographic data, there is an electron count of 114 per unit cell, which corresponds to 6.5 MeOH molecules in the unit cell of **lp-CFA-9**. Removal of the solvent by drying and/or heating the sample leads to structural changes. Due to the fact that the **lp-CFA-9** and **np-CFA-9** structures are described in different crystal systems with different space groups which do not have a direct group–subgroup relation between them, the hexagonal unit cell of **lp-CFA-9** was transformed to the orthorhombic one (see Fig. 2c–f). Direct comparison of the unit cells indicates that the structural transition from the solvated sample (**lp-CFA-9**) to a desolvated one (**np-CFA-9**) is connected with the dynamic shortening of the *a*- (from 18.23 to 18.09 Å) and *b*-lattice parameters (from 31.58 Å to 28.18 Å) and slight elongation of the *c*-parameter
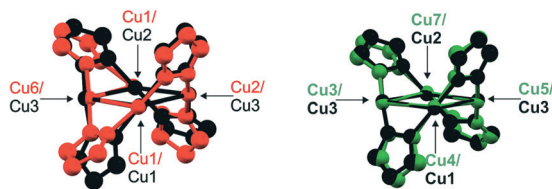
Fig. 3 Structural overlay of the SBUs of **lp-CFA-9** and **np-CFA-9** (**lp-CFA-9** – SBU in black, **np-CFA-9** – two different SBUs in red and green).

(from 16.40 to 16.72 Å). This process is accompanied by the unit cell volume change from 9442 Å^3 (**lp-CFA-9**) to 8524 Å^3 (**np-CFA-9**). The framework flexibility results from the properties of the tetraphenylbipyrazolate ligand where two pyrazolate rings can rotate around the central C–C single bond. In **lp-CFA-9**, the angle between the planes created by pyrazolate rings is 60.7°, while in **np-CFA-9** the angle value ranges from 65.0 to 65.5° (see Fig. 3). The intramolecular Cu···Cu distances in **np-CFA-9** range from 3.049(3) to 3.129(1) Å. The Cu–N distances range from 1.774(15) to 1.916(13) Å (see the ESI,† Table S1). Taking the van der Waals radii of hydrogen atoms (1.2 Å) into account, the narrowest channel diameter calculated between the hydrogen atoms of the Ph-groups in **np-CFA-9** is 4.07 Å, while the smallest aperture of the channel is 2.27 Å. Estimation using the SQUEEZE[30] program reveals that the initial solvent accessible void volume is 566.5 Å^3, or 0.046 cm^3 g^{-1}, which is 6.6% of the unit cell volume (8524.4(11) Å^3) for a probe radius of 2.07 Å,[31] corresponding to the approximate van der Waals radius of carbon dioxide.

Topology analysis using the TOPOS program[32] (see the ESI†) reveals that the **lp-CFA-9** and **np-CFA-9** coordination networks can be described as chiral **qtz** (quartz) nets by regarding the Cu$_4$pz$_4$ SBUs as four-connected nodes and the phbpz^{2-} ligands as spacers (see the ESI† and Fig. 4).

The chirality of both networks results from the D_{2d} symmetry of their SBUs. It is known that α-quartz exists in two crystal structure forms, which represent exact mirror images of each other. Taking into account that these forms are described by two different space groups $P3_121$ (no. 152, *right*-handed screw) and $P3_221$ (no. 154, *left*-handed screw), it can be concluded that **lp-CFA-9** described in the $P3_221$ (no.
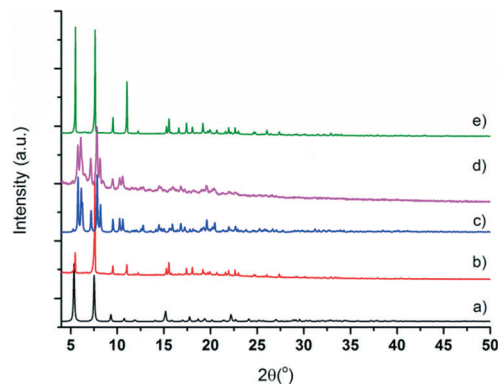

Fig. 5 Calculated and measured X-ray powder patterns for **CFA-9**. (a) Calculated pattern of **lp-CFA-9**; (b) measured pattern of **lp-CFA-9**; (c) calculated pattern of **np-CFA-9**; (d) measured pattern of **np-CFA-9**; and (e) dried sample re-solvated by DMF.

154) space group represents the *left*-handed screw.[33] Due to the fact that in the case of **np-CFA-9** two enantiomers can be described in the same $P2_12_12$ (no. 18) space group, the structure of **np-CFA-9** was transformed to the $P6_222$ (no. 180) and $P6_422$ (no. 181) space groups. From the comparison of two structures of **lp-CFA-9** $P3_221$ (no. 154) and **np-CFA-9** $P6_222$ (no. 180), it follows that the networks exhibit the same chirality. Interestingly, to the best of our knowledge, only one example of a predicted SiO$_2$ polymorph described in the $P2_12_12$ (no. 18) space group can be found in the literature.[34]

The crystal structure transformation from the solvated state to the desolvated one and back upon immersing the dried sample in polar solvents (MeOH, DEF, NMP) is dynamic and reversible, as confirmed by XRPD studies.

TGA and XRPD studies

Microcrystalline powder samples of **CFA-9** were exposed to air for a long period of time; the colour change of the sample from white to light green after several months reflects very slow oxidation of the Cu(I) ions. The phase purity of **CFA-9** was confirmed by XRPD measurement under ambient conditions. The experimental XRPD pattern of the wet sample (a) is consistent with the simulated one (b), as gleaned from the single crystal X-ray diffraction data, as shown in Fig. 5. Differences in peak intensities
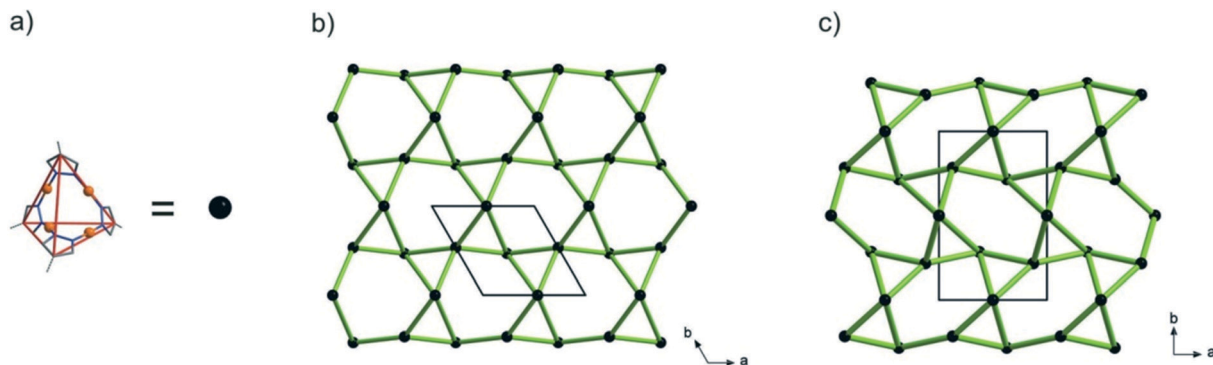

Fig. 4 (a) Simplified diagram of the SBUs of **CFA-9**. Topological representation of **lp-CFA-9** (b) and **np-CFA-9** (c).
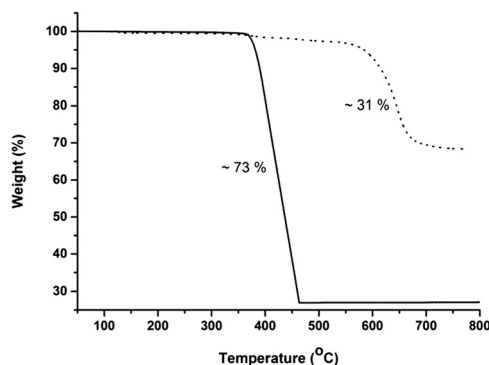
Fig. 6 Temperature-dependent weight loss of **CFA-9** under flowing nitrogen (dashed line) and oxygen (solid line) gas.

Fig. 8 CO_2 adsorption/desorption isotherms at 194.7 K for **CFA-9**.

are due to occluded solvent molecules. Similarly, the experimental XRPD pattern of the dried sample (c) is consistent with the simulated one (d), as gleaned from the single crystal X-ray diffraction data.

In addition, the thermal stability of **CFA-9** was determined by thermogravimetric (TG) and VTXRPD measurements. Prior to the measurements, the sample was heated at 100 °C under vacuum for 2 h in order to remove occluded solvent molecules (MeOH). As shown in Fig. 6, the thermogravimetric profile of **CFA-9** under nitrogen exhibits a weight loss of 31% between 570 and 650 °C, while under oxygen a weight loss of 73% occurs between 350 and 400 °C. In both cases, the steps are connected with the degradation of the compound. According to the VTXRPD data presented in Fig. 7, the sample is stable up to *ca.* 450 °C (measurement in a capillary). Above 500 °C, Cu (PDF no. 3-1015) was detected. Removal of the solvent by drying and/or heating the sample leads to XRPD pattern changes, which is connected with the structural changes of the compound. Interestingly, the XRPD pattern of the **CFA-9** sample heated at 100 °C for 0.5 h under vacuum can be recovered after the desolvated compound was taken up with polar solvents such as MeOH, EtOH, DMF, DEF or NMP, which indicates that the solvent removal is completely reversible and the initial structure can be recovered (see Fig. 5e).
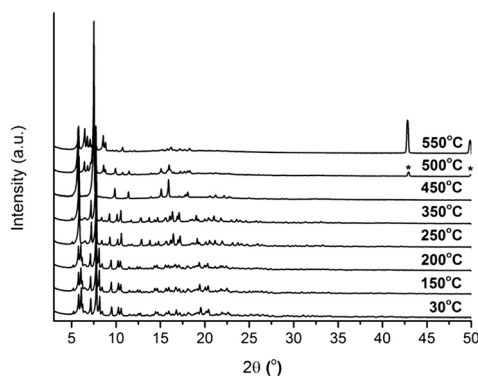
Physisorption studies

The argon adsorption isotherm for **CFA-9** measured at 87.3 K (Fig. S4†) is typical of non-porous solids and reveals a BET surface area of only 11 m^2 g^{-1}. However, the sorption measurement with CO_2 at 194.7 K reveals a much higher BET surface area of 189 m^2 g^{-1} and shows a well-pronounced hysteresis in the relative pressure range 0.15–0.3 (Fig. 8), which is typical of breathing MOFs. The pore volume of **np-CFA-9** determined from the adsorption branch of the CO_2 isotherm at $p/p_0 = 0.1$ is 0.051 cm^3 g^{-1} while the volume of **lp-CFA-9** determined from the adsorption branch of the CO_2 isotherm at $p/p_0 = 0.99$ is 0.115 cm^3 g^{-1}; both values correspond well to the calculated ones. The flexibility of the framework was additionally investigated by XRPD measurements under CO_2 atmosphere (Fig. 9).

The sample was cooled under vacuum to −78.5 °C and the pressure of CO_2 was gradually increased up to 1000 mbar (red curves in Fig. 9) and then substantially decreased (grey curves). After changing from vacuum to a CO_2 atmosphere, the intensity of the first five Bragg peaks decreased. With

Fig. 7 VTXRPD plots of **CFA-9** kept in air and sampled in a temperature range of 30–550 °C. *Cu PDF no: 3-1015.

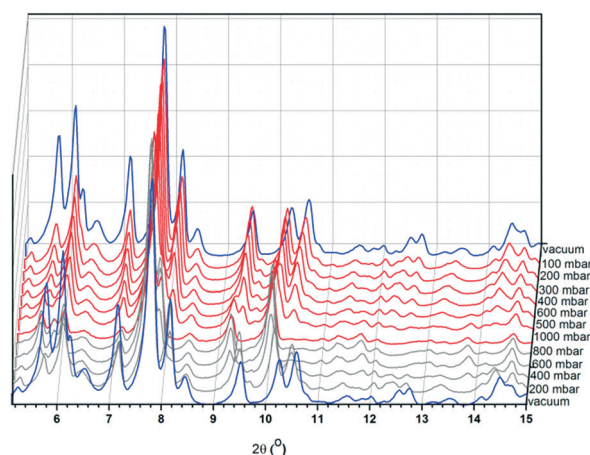**Fig. 9** XRPD plots of **CFA-9** measured at −78.5 °C under vacuum (blue lines) and under increasing CO_2 pressure (red lines) and decreasing CO_2 pressure (grey lines).
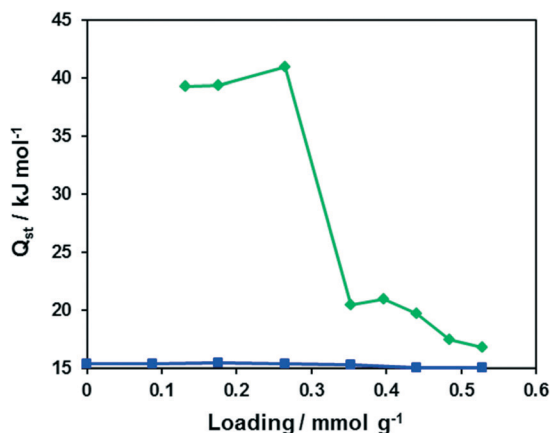
Paper

Fig. 10 Dependencies of the isosteric heats of O_2 (blue) and CO (green) adsorption on the loading for **CFA-9**.

increasing CO_2 pressure, new peaks occur (*e.g.* 9.67° 2θ at 100 mbar, 9.28° 2θ at 500 mbar, and 5.61° 2θ at 600 mbar). Next, decreasing the CO_2 pressure leads to the same XRPD pattern as the one detected under vacuum (blue patterns).

The isosteric heat of CO adsorption determined from adsorption isotherms measured in the temperature range 203–223 K (Fig. S6†) lies at approx. 40 kJ mol^{-1} at low loading (<0.3 mmol g^{-1}) and decreases to typical physisorption values of 17–20 kJ mol^{-1} at higher loading (Fig. 10). Such behaviour hints at weak binding of carbon monoxide to Cu(I) centers of **CFA-9**. Oxygen, in contrast, shows a constant physisorption heat of approx. 15 kJ mol^{-1} and thus does not bind to the Cu(I) centers.

The adsorption of CO in **CFA-9** was further studied by diffuse reflectance Fourier-transform IR spectroscopy (DRIFT). The pre-dried and activated **CFA-9** sample was heated to 100 °C under Ar and the atmosphere was changed to CO. The bands at 2170 cm^{-1} and 2125 cm^{-1} belong to free CO molecules in the gas phase (black line, Fig. 11). At 100 °C under CO atmosphere, a new band at 2102 cm^{-1} appeared. Gradu-
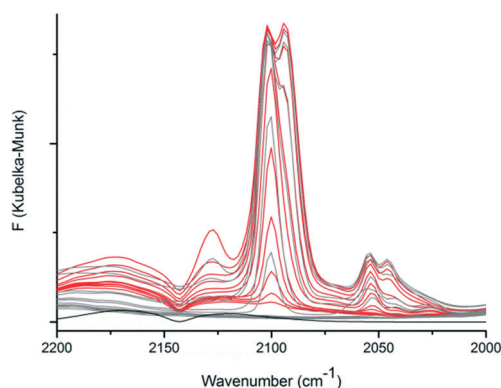

Fig. 11 *In situ* DRIFT spectra of **CFA-9** recorded in 20 °C steps upon cooling from 100 °C to −100 °C under a CO atmosphere (red lines) and subsequent heating from −100 °C to 100 °C under an Ar atmosphere (gray lines). The DRIFT spectrum of KBr at −60 °C under a CO atmosphere (black line).
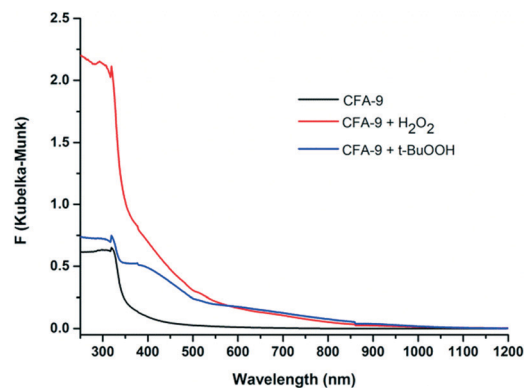

Fig. 12 UV-vis spectra of **CFA-9** at room temperature. Black line – **CFA-9**, red – **CFA-9** oxidized by H_2O_2, blue – **CFA-9** oxidized by *t*-BuOOH.
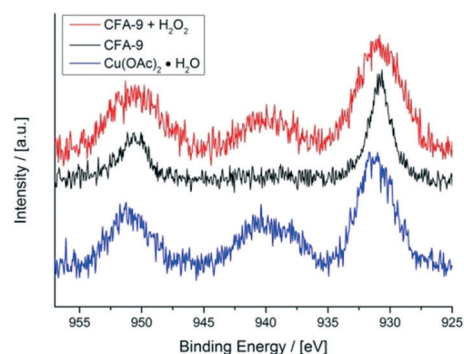
Fig. 13 XPS spectra of the Cu2p$_{1/2}$ and Cu2p$_{3/2}$ regions of **CFA-9** (black), **CFA-9** oxidized by H_2O_2 (red), and Cu(OAc)$_2$ (blue).

ally decreasing the temperature in 20 °C steps led to the increase in the intensity of this band until a new weak band at 2050 cm^{-1} was detected at 40 °C. The corresponding spectra (red lines) are presented in Fig. 11. At −40 °C, the splitting of the band at 2102 cm^{-1} was observed and a new additional band centered at 2094 cm^{-1} was registered. Subsequent lowering of the temperature led to increasing intensities of the bands at 2102 and 2094 cm^{-1} and the appearance of new bands at 2127 and 2046 cm^{-1}. At −100 °C, the atmosphere was changed to Ar, and after 1 h the sample was gradually heated up to 100 °C. The corresponding spectra (gray lines) are presented in Fig. 11. With increasing temperature, the bands at 2127, 2094 and 2046 cm^{-1} gradually decreased in intensity, and at −40 °C the main bands

Fig. 14 Peak shape analysis of the Cu2p$_{3/2}$ peaks of a) **CFA-9** (FWHM = 2.2 eV) and b) **CFA-9** oxidized by H_2O_2 (FWHM = 4.4 eV).

Fig. 15 XRPD measurements of **CFA-9** after reaction with Br$_2$.

at 2102 and 2053 cm^{-1} were observed. Subsequent rising of the temperature led to complete vanishing of these bands at 20 °C. All these recorded bands correspond to the stretch mode of 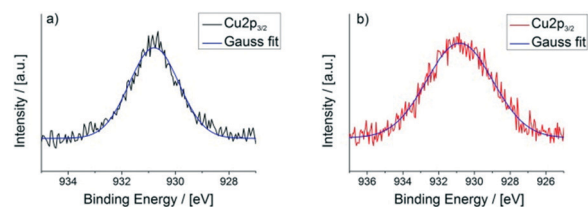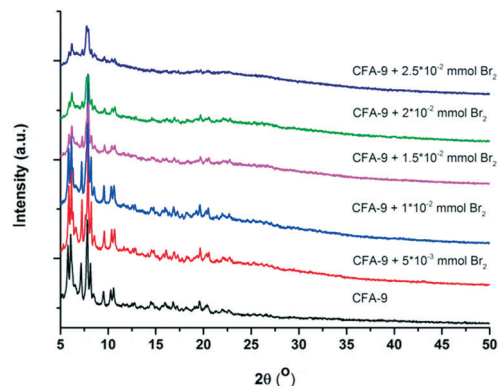the CO molecule coordinatively bound to Cu^I–ions and are in good agreement with literature data: νCO = 2137 cm^{-1} for [Cu{HB(3,5-(CF$_3$)$_2$pz)$_3$}(CO)],[35] 2102 cm^{-1} for [Cu{HB(3-C$_3$F$_7$pz)$_3$}(CO)],[36] 2056 cm^{-1} for [Cu{HB(3,5-iPr$_2$pz)$_3$}(CO)][37] and 2043–2063 cm^{-1} for hemocyanin.[38]

In order to prove the reactivity of **CFA-9** towards oxidizing reagents, the compound was oxidized by H$_2$O$_2$ or *t*-BuOOH and investigated by UV-vis spectroscopy. The solid-state UV-vis spectrum of **CFA-9** displays one strong absorption peak at 318 nm in the UV region, which could be assigned to the intraligand electron transitions (Fig. 12). The UV-vis spectra of **CFA-9** samples, oxidized by H$_2$O$_2$ or *t*-BuOOH, exhibit one additional broad peak with the maximum centered at *ca.* 600 nm, which encompasses the Cu^{II} d–d transitions.[39] The XRPD patterns of the oxidized samples are similar to that of the **CFA-9** sample (see Fig. S2†). Furthermore, the oxidized **CFA-9** sample

Table 1 Br : Cu ratios in the products obtained from the reaction of **CFA-9** with Br$_2$

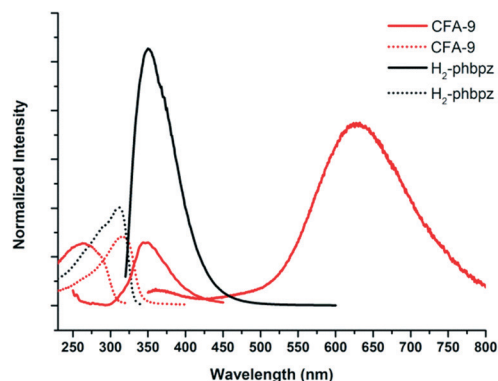| Initial molar ratio Br$_2$: Cu	Br : Cu ratio in the product
1 : 2	0.34
1 : 1	0.51
1.5 : 1	0.62
2 : 1	0.67
2.5 : 1	0.95

Fig. 16 Solid-state photoluminescence spectra of **CFA-9** and the H$_2$-phbpz ligand at room temperature. Dashed-lines – excitation spectra, continuous-lines – emission spectra.

can be reduced back to a Cu(I)-MOF upon heating in DMF at 120 °C for 4 h. The XRPD pattern is also similar to that of the **CFA-9** sample, indicating that the structure remains stable during this oxidation/reduction sequence.

X-ray photoelectron spectroscopy (XPS) further proves the redox activity of **CFA-9**. Fig. 13 depicts the XPS spectrum of **CFA-9** oxidized by H$_2$O$_2$, which shows a prominent satellite feature at about 940 eV between the two Cu2p peaks. This

Table 2 Emission and excitation data for pyrazolato compounds at r.t

Compound	Emission λ_{max} (excited) (nm)	Cu–Cu shortest distance (Å)
CFA-9	631, 360 (312)	3.049(3)$_{(intra)}$, 8.266(2)$_{(inter)}$
CFA-2 (ref. 26)	468 (381)	3.192(2)$_{(intra)}$, 7.651$_{(inter)}$
[Cu(μ-3,5-iPr$_2$pz)]$_3$ (ref. 42b)	577 (280)	3.0250(7)$_{(inter)}$, 3.1907(6)$_{(intra)}$
[Cu(μ-3-tBu-5-iPrpz)]$_4$ (ref. 42b)	556.5 (280)	3.071(2)$_{(intra)}$
[Cu(μ-3,5-tBu$_2$pz)]$_4$ (ref. 42c)	544.5 (280)	3.1325(6)$_{(intra)}$
[Cu(μ-3,5-Me$_2$pz)]$_3$ (ref. 42c)	656 (304)	3.195$_{(intra)}$, 2.946$_{(inter)}$
[Cu(μ-3,5-(CF$_3$)$_2$pz)]$_3$ (ref. 42c)	645 (306)	3.218$_{(intra)}$, 3.813(1)$_{(inter)}$
[Cu(μ-3-(CF$_3$)pz)]$_3$ (ref. 42c)	659 (306)	3.214$_{(intra)}$, 3.100$_{(inter)}$
[Cu(μ-3-(CF$_3$)-5-Mepz)]$_3$ (ref. 42c)	634 (345)	3.201$_{(intra)}$, 3.704$_{(inter)}$
[Cu(pz)]$_3$ (ref. 44)	542 (305)	2.954$_{(inter)}$, 3.194$_{(intra)}$
[Cu$_2$(bpz)]$_n$ (ref. 44)	598 (305)	3.331$_{(inter)}$, 3.022$_{(intra)}$
{[4-Cl-3,5-(CF$_3$)$_2$pz]Cu}$_3$ (ref. 45)	574 (280)	3.210$_{(intra)}$
{[4-Br-3,5-(CF$_3$)$_2$pz]Cu}$_3$ (ref. 45)	585 (300)	3.214$_{(intra)}$
{CuCl[CuL]$_3$}$_n$ (ref. 46)	476 (355)	3.103(1)$_{(intra)}$
{CuBr[CuL]$_3$}$_n$ (ref. 46)	536 (397)	3.094(2)$_{(intra)}$, 5.120(3)$_{(inter)}$
{CuI[CuL]$_3$}$_n$ (ref. 46)	525 (400)	3.126(1)$_{(intra)}$, 3.311$_{(inter)}$
{CuSCN[CuL]$_3$(MeCN)}$_n$ (ref. 46)	560 (405)	3.109(1)$_{(intra)}$, 3.368(1)$_{(inter)}$
{Cu$_2$I$_2$[CuL]$_3$}$_n$ (ref. 46)	482 (397)	3.100(1)$_{(intra)}$
[Cu(ppz)]$_3$ (ref. 47)	564 (300)	3.172$_{(intra)}$, 3.439$_{(inter)}$
{[Cu(ppz)]$_3$[CuCN]$_3$} (ref. 47)	494 (360)	3.128$_{(intra)}$, 3.317$_{(inter)}$

HL = 3,5-diethyl-4-(4-pyridyl)-pyrazole.

Table 3 Crystal data and structure refinements of **lp**- and **np-CFA-9**

Compound	lp-CFA-9·MeOH	np-CFA-9
Empirical formula	$C_{31}H_{24}Cu_2N_4O$	$C_{30}H_{20}Cu_2N_4$
Formula	$Cu_2C_{30}H_{20}N_4 \cdot MeOH$	$Cu_2C_{30}H_{20}N_4$
M_r/g mol^{-1}	595.62	563.58
T/K	100(2)	296(2)
Wavelength/Å	0.71073	0.71073
Crystal system	Trigonal	Orthorhombic
Space group	$P3_221$ (no. 154)	$P2_12_12$ (no. 18)
a/Å	18.2348(6)	18.0922(15)
b/Å	18.2348(6)	28.182(2)
c/Å	16.3950(4)	16.7188(12)
V/Å^3	4721.1(2)	8524.4(11)
Z	6	12
D_c/g cm^{-3}	1.257	1.437
μ/mm^{-1}	1.378	1.530
$F(000)$	1824	3778
θ range/°	2.56 to 25.02	2.20 to 25.07
Refls. collected	36 249	126 433
Refls. unique	5569	15 080
$R_{(int)}$	0.0363	0.2354
GooF	1.059	1.426
Flack parameter	0.02(2)	0.12(5)
R_1 [$I > 2\sigma(I)$]^a	0.0409	0.1496
wR_2 (all data)^b	0.1129	0.3181
Largest diff. peak and hole/Å^{-3}	0.799 and −0.274	1.157 and −0.947

^{a} $R_1 = \sum ||F_0| - |F_c||/\sum|F_0|$. ^{b} w$R_2 = \sum[w(F_0^2 - F_c^2)2]/\sum[w(F_0^2)2]^{1/2}$.

characteristic maximum is only present for Cu(II) species,[40] *e.g.* Cu(OAc)$_2$. The XPS spectrum of the as-synthesized **CFA-9** shows only the Cu2p$_{1/2}$ and Cu2p$_{3/2}$ peaks at about 951 eV and 931 eV. Peak shape analysis of the Cu2p$_{3/2}$ peaks of **CFA-9** and oxidized **CFA-9** also speaks in favour of Cu(I) for the former and Cu(II) for the latter (see Fig. 14).[41]

Additionally, the reactivity of **CFA-9** towards Br$_2$ was investigated. 11.3 mg (0.01 mmol) of the sample was added to solutions of Br$_2$ in CH$_2$Cl$_2$ (0.005, 0.01, 0.015, 0.02 and 0.05 mmol) and stirred for 15 minutes at r. t. The color of the samples changed from colorless to brown. Then, the samples were filtered off by suction, washed thoroughly with MeOH and dried. The samples were analyzed by EDX spectroscopy (Table 1) and X-ray diffraction (Fig. 15). Several attempts were undertaken to perform single-crystal X-ray diffraction measurements. Unfortunately, the quality of the Br$_2$-treated crystals was not sufficient for the measurement. Instead, the samples were investigated by powder X-ray diffraction. The measurements show that the crystallinity of the framework is completely retained only when a 1 : 1 Br$_2$/Cu ratio was applied. In this case, a product with an approx. Br/Cu ratio of 0.5 was obtained. Applying a higher initial Br$_2$/Cu ratio allows the increase in the Br/Cu ratio in the product, but also leads to subsequent degradation of the framework.

Photoluminescence

Pyrazolate-bridged complexes containing Cu(I) ions with d^{10} closed-shell electronic configuration are known to show luminescence.[42] Upon irradiation with UV light, Cu(I) pyrazolates undergo a metal-to-ligand charge transfer resulting in a charge separated excited singlet state. This state can either decay to the ground state by emission of slightly red-shifted light, or undergo spin conversion into an excited triplet state, which shows slow decay (luminescence) to the ground state.[43] The latter transition might be influenced by weak Cu···Cu interactions that typically occur in Cu(I) complexes and coordination polymers comprising bridging pyrazolate moieties. The usually broad luminescence band for Cu(I) pyrazolates is observed between *ca.* 460 and 660 nm (see Table 2). **CFA-9** irradiated at 312 nm gave two broad emission bands with the maxima at 360 and 631 nm (Fig. 16). The luminescence behaviour of **CFA-9** was almost the same as those previously reported in the literature and results from intramolecular Cu···Cu interactions (3.049(3)$_{(intra)}$ and 8.266(2)$_{(inter)}$ Cu···Cu distances in **CFA-9**).

Conclusions

The work reported here focuses on the synthesis and characterization of a chiral metal–organic framework assembled from tetranuclear Cu(I) secondary building units and 3,3′,5,5′-tetraphenylbipyrazolate ligands. **CFA-9** exhibits breathing effects upon exposure to different kinds of polar liquids (MeOH, EtOH, DMF, DEF, NMP), whereas non-polar solvents are not taken up at all. The framework flexibility results from the properties of the tetraphenylbipyrazolate ligand where two pyrazolate rings can rotate around the central C–C single bond. The interplanar angle changes from 60.7° (fully solvated state, **lp-CFA-9**) to 65.0–65.5° (fully desolvated form, **np-CFA-9**). The structural dynamics accompanying solvent removal and uptake in **CFA-9** are connected with the changes

of the crystal system from hexagonal to orthorhombic (**np-CFA-9** phase) and back to hexagonal (**lp-CFA-9** phase), respectively. The weak chemisorption of carbon monoxide on Cu(I) centers was confirmed by sorption and IR measurements, whereas no chemisorption of oxygen was observed. The reactions of **CFA-9** with H_2O_2 or *t*-BuOOH indicate that the MOF is stable during repeated oxidation/reduction sequences.

Experimental

Materials and general methods

Commercially available reagents of analytical grade were used as received without further purification.

Synthesis of CFA-9

Solvothermal method. A mixture of Cu(OAc)$_2$·H$_2$O (8 mg, 0.04 mmol) and H$_2$-phbpz (30 mg, 0.06 mmol) was dissolved in MeOH (4 mL). 2,6-Dimethylpyridine (2,6-lutidine) (0.05 mL) was added and the solution was placed in a glass tube (10 mL). The tube was closed with a cap and heated at 120 °C for 3 d and then subsequently cooled to room temperature. The colourless crystals were filtered off by suction and washed thoroughly with MeOH. The synthesis can be similarly performed at larger quantities (upscale factor: 50). Yield: 7 mg, 29% (based on Cu(OAc)$_2$·H$_2$O). IR: (cm^{-1}) 473 w, 486 w, 503 w, 570 w, 609 w, 649 m, 691 vs, 718 s, 746 s, 756 s, 782 s, 792 w, 837 w, 908 w, 1015 m, 1072 w, 1119 m, 1157 w, 1176 w, 1297 w, 1319 w, 1334 w, 1415 w, 1447 s, 1467 m, 1511 w, 1575 w, 1601 w, 1746 w, 1868 w, 1868 w, 1942 w, 2050 w. The IR spectrum of **CFA-9** is shown in Fig. S3.†

Microwave irradiation method. A mixture of Cu(OAc)$_2$·H$_2$O (8 mg, 0.04 mmol) and H$_2$-phbpz (30 mg, 0.06 mmol) was dissolved in MeOH (3 mL). 2,6-Dimethylpyridine (2,6-lutidine) (0.05 mL) was added and the solution was placed in a Pyrex sample tube (10 mL). The tube was closed with a cap and placed in a microwave synthesizer (CEM, Discover S). The resulting mixture was heated to 150 °C at 300 W for 25 min and then cooled to room temperature. The colourless microcrystalline material was filtered off by suction and washed thoroughly with MeOH. The synthesis can be similarly performed at larger quantities (upscale factor: 50). Yield: 8 mg, 33% (based on Cu(OAc)$_2$·H$_2$O). This material exhibited the same analytical results as the one obtained by the solvothermal method.

Physical methods. Fourier transform infrared (FTIR) spectra were recorded with ATR unit in the range 4000–400 cm^{-1} on a Bruker Equinox 55 FT-IR spectrometer. The following indicators are used to characterize absorption bands: very strong (vs), strong (s), medium (m), weak (w). Thermogravimetric analysis (TGA) was performed using a TGA Q500 analyzer in the temperature range of 25–800 °C in flowing nitrogen at a heating rate of 10 K min^{-1}. Ar, CO, CO$_2$ and O$_2$ sorption isotherms were measured using a BELSORP-max instrument combined with a BELCryo system. The amounts of adsorbed gas are given in cm^3 g^{-1} [STP], where STP = 101.3 kPa and 273.15 K. Prior to measurements, the

sample was heated at 100 °C for 2 h under high vacuum in order to remove occluded solvent molecules. Ambient temperature X-ray powder diffraction (XRPD) patterns were measured using a Seifert XRD 3003 TT diffractometer equipped with a Meteor 1D detector operated at 40 kV, 40 mA, and CuK$_\alpha$ (λ = 1.54247 Å) with a scan speed of 10 s per step and a step size of 0.02° in 2θ. The variable temperature XRPD data were collected in the 2θ range of 5–60° with 0.02° steps, using a Bruker D8 Advance diffractometer equipped with a Lynxeye linear position-sensitive detector, an MRI TCPU1 oven, in transmission geometry. The sample was loaded into a capillary (Hilgenberg) made from special glass no. 10, with 0.5 mm diameter and 0.01 mm wall thickness. The patterns were recorded in a temperature range from 30 to 250 °C, in the 5–60° 2θ range, with one step per 1 s and an angular step width of 0.02° in 2θ. The temperature program between measurements is as follows: a heating rate of 0.5 °C s^{-1} and then 10 min isothermal. The XRPD data under CO$_2$ pressure were collected using an Empyrean (PANalytical) Diffractometer equipped with a Bragg–Brentano^{HD} mirror, a PIXcel^{3D} 2 × 2 detector and a Cryo & humidity Chamber CHC plus$^+$ (Anton Paar). The sample was cooled under vacuum to −78.5 °C. Next, the pressure of CO$_2$ was gradually increased up to 1000 mbar and then substantially decreased. The patterns were recorded in the 4–50° 2θ range, with one step per 185.4 s and an angular step width of 0.03° in 2θ. The diffuse reflectance Fourier-transform IR spectra (DRIFT) were collected between 3500–400 cm^{-1} using an Equinox 55 FT-IR spectrometer equipped with a Praying Mantis diffuse reflectance accessory and an environmental chamber (Harrick Scientific Products) and referenced to KBr. X-ray photoelectron spectra (XPS) were obtained by employing an Omicron spectrometer featuring a monochromatic Mg anode (XM 1000 Mk II, 1486.7 eV) and a hemispherical analyzer (EA 125). Each spectrum was collected from 925 to 960 eV with 120 to 160 sweeps. Energy-dispersive X-ray spectroscopy (EDX) was performed using a Philips XL 30 FEG scanning electron microscope equipped with an EDAX SiLi detector. Luminescence spectra were acquired using a spectrofluorimeter (FS920, Edinburgh Instruments) equipped with a TMS300 monochromator, an S900 single photon photomultiplier, and a Xe 900 450 W xenon arc lamp at r. t. The excitation and emission spectra were corrected for the wavelength-dependent lamp intensity and detector response, respectively.

Single-crystal X-ray diffraction. The crystal of **lp-CFA-9** was collected from the mother liquor and mounted on a MiTeGen MicroMounts. The sample **CFA-9** was dried in air and several crystals of **np-CFA-9** were mounted on a MiTeGen MicroMounts and tested using a diffractometer. Unfortunately, most of the crystals scattered only up to 32° 2θ (1.3 Å resolution). Most of the dried crystals were cracked (see the SEM picture, Fig. 1). The best recorded data were obtained for a single crystal of **np-CFA-9** with approx. dimensions of 121 × 49 × 66 μm^3. X-ray data for the single crystal structure determinations of **lp-** and **np-CFA-9** were collected using a Bruker D8 Venture diffractometer. Intensity measurements were

performed using monochromated (doubly curved silicon crystal) MoKα radiation (0.71073 Å) from a sealed microfocus tube. The generator settings were 50 kV and 1 mA. The data collection temperature was −173 °C. APEX2 software was used for the preliminary determination of the unit cell.[48] The determination of integrated intensities and unit cell refinement was performed using SAINT.[49] The structures were solved and refined using the Bruker SHELXTL Software Package.[50] Selected crystal data and details of structure refinements are provided in Table 3.

Acknowledgements

Notes and references

1 (a) J. Liu, L. Chen, H. Cui, J. Zhang, L. Zhang and C.-Y. Su, *Chem. Soc. Rev.*, 2014, **43**, 6011; (b) K. Leus, Y.-Y. Liu and P. Van Der Voort, *Catal. Rev.: Sci. Eng.*, 2014, **56**, 1; (c) P. Silva, S. M. F. Vilela, J. P. C. Tomé and F. A. A. Paz, *Chem. Soc. Rev.*, 2015, **44**, 6774.

2 (a) J. Ren, H. W. Langmi, B. C. North and M. Mathe, *Int. J. Energy Res.*, 2015, **39**, 607; (b) D. Banerjee, A. J. Cairns, J. Liu, R. K. Motkuri, S. K. Nune, C. A. Fernandez, R. Krishna, D. M. Strachan and P. K. Thallapally, *Acc. Chem. Res.*, 2015, **48**, 211; (c) H. Furukawa, K. E. Cordova, M. O'Keeffe and O. M. Yaghi, *Science*, 2013, **341**, 974.

3 M. Giménez-Marqués, T. Hidalgo, C. Serre and P. Horcajada, *Coord. Chem. Rev.*, 2016, **307**, 342.

4 (a) L. Wang, Y. Han, X. Feng, J. Zhou, P. Qi and B. Wang, *Coord. Chem. Rev.*, 2016, **307**, 361; (b) M. R. Ryder and J.-C. Tan, *Mater. Sci. Technol.*, 2014, **30**, 13a.

5 A. Schneemann, V. Bon, I. Schwedler, I. Senkovska, S. Kaskel and R. A. Fischer, *Chem. Soc. Rev.*, 2014, **43**, 6062.

6 (a) C. R. Murdock, B. C. Hughes, Z. Lu and D. M. Jenkins, *Coord. Chem. Rev.*, 2014, **258–259**, 119; (b) G. Férey, *Chem. Soc. Rev.*, 2008, **37**, 191.

7 SciFinder, American Chemical Society, 2016.

8 PubMed, National Center for Biotechnology Information, U. S. National Library of Medicine.

9 Web of Science, Thomson Reuters, 2015.

10 B. Mu, F. Li, Y. Huang and K. S. Walton, *J. Mater. Chem.*, 2012, **22**, 10172.

11 D. L. Reger, A. Leitner, P. J. Pellechia and M. D. Smith, *Inorg. Chem.*, 2014, **53**, 9932.

12 (a) L. Ma, C. Abney and W. Lin, *Chem. Soc. Rev.*, 2009, **38**, 1248; (b) J. D. Evans and F.-X. Coudert, *J. Am. Chem. Soc.*, 2016, **138**, 6131; (c) T. Sawano, P. Ji, A. R. McIsaac, Z. Lin, C. W. Abney and W. Lin, *Chem. Sci.*, 2015, **6**, 7163.

13 (a) Y. Cui, B. Li, H. He, W. Zhou, B. Chen and G. Qian, *Acc. Chem. Res.*, 2016, **49**(3), 483; (b) M. Zhang, X. Chen, J. Zhang, J. Kong and L. Yuan, *Chirality*, 2016, **28**(4), 340.

14 (a) O. R. Evans and W. B. Lin, *Acc. Chem. Res.*, 2002, **35**, 511; (b) C. Wang, T. Zhang and W. Lin, *Chem. Rev.*, 2012, **112**, 1084.

15 (a) C.-L. Chang, X.-Y. Qi, J.-W. Zhang, Y.-M. Qiu, X.-J. Li, X. Wang, Y. Bai, J.-L. Sun and H.-W. Liu, *Chem. Commun.*, 2015, **51**, 3566; (b) Z. Chen, X. Liu, C. Zhang, Z. Zhang and F. Liang, *Dalton Trans.*, 2011, **40**, 1911.

16 L. Que and W. B. Tolman, *Nature*, 2008, **455**, 333.

17 L. Jian, C. Chen, F. Lan, S. Deng, W. Xiao and N. Zhang, *Solid State Sci.*, 2011, **13**, 1127.

18 D. Jiang, T. Mallat, F. Krumeich and A. Baiker, *J. Catal.*, 2008, **275**, 390.

19 D. Jiang, T. Mallat, D. M. Meier, A. Urakawa and A. Baiker, *J. Catal.*, 2010, **270**, 26.

20 N. T. S. Phan, P. H. L. Vu and T. T. Nguyen, *J. Catal.*, 2013, **306**, 38.

21 (a) S. Marx, W. Kleist and A. Baiker, *J. Catal.*, 2011, **281**, 76; (b) F. X. Llabres i Xamena, O. Casanova, R. Galiasso Tailleur, H. Garcia and A. Corma, *J. Catal.*, 2008, **255**, 220; (c) S. Wang, L. Li, J. Zhang, X. Yuan and C.-Y. Su, *J. Mater. Chem.*, 2011, **21**, 7098.

22 C. Huang, J. Wu, C. Song, R. Ding, Y. Qiao, H. Hou, J. Chang and Y. Fan, *Chem. Commun.*, 2015, **51**, 10353.

23 (a) P.-Q. Liao, C.-T. He, D.-D. Zhou, J.-P. Zhang and X.-M. Chen, in *The Chemistry of Metal–Organic Frameworks: Synthesis, Characterization and Applications*, ed. S. Kaskel, Wiley, Weinheim, Germany, 2016, ch. 11, pp. 309–343; (b) C. Pettinari, A. Tăbăcaru and S. Galli, *Coord. Chem. Rev.*, 2016, **307**, 1–31; (c) J.-P. Zhang, Y.-B. Zhang, J.-B. Lin and X.-M. Chen, *Chem. Rev.*, 2012, **112**, 1001.

24 M. Grzywa, C. Geßner, B. Bredenkötter, D. Denysenko, J. van Leusen, P. Kögerler, E. Klemm and D. Volkmer, *Dalton Trans.*, 2014, **43**, 16846.

25 D. Denysenko, M. Grzywa, J. Jelic, K. Reuter and D. Volkmer, *Angew. Chem., Int. Ed.*, 2014, **53**, 5832.

26 M. Grzywa, C. Geßner, D. Denysenko, B. Bredenkötter, F. Gschwind, K. M. Fromm, W. Nitek, E. Klemm and D. Volkmer, *Dalton Trans.*, 2013, **42**, 6909.

27 (a) J.-X. Zhang, T.-T. Yan, J.-F. Kou, W.-H. Zhang and G. Yang, *Z. Naturforsch., B: J. Chem. Sci.*, 2015, **70**, 59; (b) A. Tăbăcaru, C. Pettinari, I. Timokhin, F. Marchetti, F. Carrasco-Marín, F. J. Maldonado-Hódar, S. Galli and N. Masciocchi, *Cryst. Growth Des.*, 2013, **13**, 3087.

28 J.-H. Wang, M. Li and D. Li, *Chem. – Eur. J.*, 2014, **20**, 12004.

29 J. P. Freeman and J. F. Hansen, *J. Chem. Soc., Chem. Commun.*, 1972, 961.

30 A. L. Spek, *J. Appl. Crystallogr.*, 2003, **36**, 7.

31 W. M. Haynes, *Handbook of Chemistry and Physics*, CRC Press, Cleveland, 2013.

32 V. A. Blatov, *IUCr CompComm Newsletter*, 2006, vol. 7, pp. 4–38.

33 Y. Tanaka, T. Kojima, Y. Takata, A. Chainani, S. W. Lovesey, K. S. Knight, T. Takeuchi, M. Oura, Y. Senba, H. Ohashi and S. Shin, *Phys. Rev. B: Condens. Matter Mater. Phys.*, 2010, **81**, 144104.

34 J. C. Wojdeł, M. A. Zwijnenburg and S. T. Bromley, *Chem. Mater.*, 2006, **18**, 1464.

35 H. V. R. Dias and H.-L. Lu, *Inorg. Chem.*, 1995, **34**, 5380.

36 H. V. R. Dias and H.-J. Kim, *Organometallics*, 1996, **15**, 5374.

37 K. Fujisawa, T. Ono, Y. Ishikawa, N. Amir, Y. Miyashita, K. Okamoto and N. Lehnert, *Inorg. Chem.*, 2006, **45**, 1698.

38 L. Y. Fager and J. O. Alben, *Biochemistry*, 1972, **11**, 4786.

39 (*a*) F. G. Mutti, M. Gullotti, L. Casella, L. Santagostini, R. Pagliarin, K. K. Andersson, M. F. Iozzi and G. Zoppellaro, *Dalton Trans.*, 2011, **40**, 5436; (*b*) C. Di Nicola, Y. Y. Karabach, A. M. Kirillov, M. Monari, L. Pandolfo, C. Pettinari and A. J. L. Pombeiro, *Inorg. Chem.*, 2007, **46**, 221.

40 (*a*) M. C. Biesinger, L. W. M. Lau, A. R. Gerson and R. St. C. Smart, *Appl. Surf. Sci.*, 2010, **257**, 887; (*b*) C. Huang, J. Wu, C. Song, R. Ding, Y. Quiao, H. Hou, J. Chang and Y. Fan, *Chem. Comm.*, 2015, **51**, 10353; (*c*) A. S. Duke, E. A. Dolgopolova, R. P. Galhenage, S. C. Ammal, A. Heyden, M. D. Smith, D. A. Chen and N. B. Shustova, *J. Phys. Chem. C*, 2015, **119**, 27457.

41 E. S. Shpiro, W. Grünert, R. W. Joyner and G. N. Baeva, *Catal. Lett.*, 1994, **24**, 159.

42 (*a*) Y. Cui, Y. Yue, G. Qian and B. Chen, *Chem. Rev.*, 2012, **112**, 1126; (*b*) K. Fujisawa, Y. Ishikawa, Y. Miyashita and K. Okamoto, *Inorg. Chim. Acta*, 2010, **363**, 2977; (*c*) H. V. R. Dias, H. V. K. Diyabalanage, M. G. Eldabaja, O.

Elbjeirami, M. A. Rawashdeh-Omary and M. A. Omary, *J. Am. Chem. Soc.*, 2005, **127**, 7489; (*d*) Q. Xiao, J. Zheng, M. Li, S.-Z. Zhan, J.-H. Wang and D. Li, *Inorg. Chem.*, 2014, **53**, 11604.

43 (*a*) N. Armaroli, G. Accorsi, F. Cardinali and A. Listorti, in *Curr Chem*, ed. V. Balzani and S. Campagna, Springer-Verlag, Berlin Heidelberg, Germany, 2007, vol. 280, pp. 69–115; (*b*) P. C. Ford, W. Cariati and J. Bourassa, *Chem. Rev.*, 1999, **99**, 3625.

44 J. He, Y.-G. Yin, T. Wu, D. Li and X.-C. Huang, *Chem. Comm.*, 2006, 2845.

45 C. V. Hettiarachchi, M. A. Rawashdeh-Omary, D. Korir, J. Kohistani, M. Yousufuddin and H. V. R. Dias, *Inorg. Chem.*, 2013, **52**, 13576.

46 L. Hou, W.-J. Shi, Y.-Y. Wang, H.-H. Wang, L. Cui, P.-X. Chen and Q.-Z. Shi, *Inorg. Chem.*, 2011, **50**, 261.

47 J.-X. Zhang, J. He, Y.-G. Yin, M.-H. Hu, D. Li and X.-C. Huang, *Inorg. Chem.*, 2008, **47**, 3471.

48 *APEX2 Version 2011.6*, Bruker AXS Inc.

49 *SAINT Version 8.32B*, Bruker AXS Inc., 2013.

50 XL Version 2013/3, G. M. Sheldrick, *Acta Crystallogr., Sect. A: Found. Crystallogr.*, 2008, **64**, 112.